PHYSICAL REVIEW B **87**, 205404 (2013)

Optical absorption in twisted bilayer graphene

Pilkyung Moon and Mikito Koshino
Department of Physics, Tohoku University, Sendai 980–8578, Japan

(Received 25 February 2013; revised manuscript received 22 April 2013; published 2 May 2013)

We theoretically study the optical absorption property of twisted bilayer graphenes with various stacking geometries and demonstrate that the spectroscopic characteristics serve as a fingerprint to identify the rotation angle between two layers. We find that the absorption spectrum almost continuously evolves in changing the rotation angle, regardless of the lattice commensurability. The spectrum is characterized by series of peaks associated with the van Hove singularity, and the peak energies systematically shift with the rotation angle. We calculate the optical absorption in two frameworks: the tight-binding model and the effective continuum model based on the Dirac equation. For small rotation angles, less than 10°, the effective model well reproduces the low-energy band structure and the optical conductivity of the tight-binding model and, also, explains the optical selection rule analytically in terms of the symmetry of the effective Hamiltonian.

DOI: 10.1103/PhysRevB.87.205404 PACS number(s): 71.20.−b, 73.22.Pr, 78.67.−n, 78.67.Wj

I. INTRODUCTION

Recent advances in fabrication of atomically thin materials[1–5] have realized a new kind of two-dimensional superlattice in which the lattice mismatch between neighboring layers gives rise to an additional potential modulation. One example of such systems is twisted bilayer graphene (TBG), in which two graphene layers are stacked in an arbitrary orientation.[1,6–10] In TBG, the interlayer interaction between two misoriented layers significantly modifies the low-energy band structure, creating novel electronic features distinct from intrinsic graphene. In decreasing the rotation angle, the interference between two lattice periods produces a Moiré pattern with a long wavelength, where the characteristic features such as band gaps and van Hove singularity appear in the far-infrared region, and the band velocity of Dirac cone is significantly reduced.[2,7,11–16] Recently, the band properties of TBG have been probed by Raman spectroscopy,[2,17–20] optical spectroscopy,[20,21] angle-resolved photoemission spectroscopy,[22] and terahertz time-domain spectroscopy.[23]

The purpose of this paper is to reveal the optical absorption properties of TBGs with various stacking geometries. The optical absorption measurement is widely adopted for graphene-based systems to investigate the electronic structures.[24–35] Theoretically, the optical absorption for light incident perpendicular to the layer is related to the dynamical conductivity, and it was calculated for monolayer graphene,[36–39] AB-stacked graphene bilayer and multilayers,[40–45] and also TBG at a specific rotation angle.[21,46,47] In particular, a recent theoretical work calculated the dynamical conductivity of a TBG using two-mode approximation, considering two Dirac cones separated by the primitive superlattice wave vector.[47]

In this paper, we calculate the optical absorption in various TBGs with a wide range of rotation angles and demonstrate that the spectroscopic characteristics serve as a fingerprint to identify the stacking angle. Here the dynamical conductivity is calculated in two different frameworks: the tight-binding model and the effective continuum model based on the Dirac equation, in both of which the effect of the periodic potential is fully taken into account. For the latter, we develop a general treatment to derive the effective model from arbitrary tight-binding parametrization. We find that the spectrum is characterized by series of peaks associated with the van Hove singularity, of which the transition energy continuously shifts as the rotation angle is changed. For small rotation angles, less than 10°, the effective model nicely reproduces the low-energy band structure and the dynamical conductivity of the tight-binding model. It also explains the optical selection rule analytically in terms of the symmetry of the effective Hamiltonian.

II. THEORETICAL METHODS

A. Atomic structure and Brillouin zone

Graphene is a single layer of carbon atoms arranged in a honeycomb lattice structure, whose unit cell includes two inequivalent sublattice sites, A and B. The stacking geometry of bilayer graphene is characterized by the relative rotation angle θ combined with the lateral translation $\boldsymbol{\delta}$ between the layers. Here we define the structure of TBG by rotating layers 1 and 2 of the AA-stacked bilayer around a common B site by $-\theta/2$ and $+\theta/2$, respectively, and then translating layer 2 relative to layer 1 by $\boldsymbol{\delta}$. We define $\mathbf{a}_1 = a(1,0)$ and $\mathbf{a}_2 = a(1/2,\sqrt{3}/2)$ as the lattice vectors of the AA-stacked bilayer before the rotation, where $a \approx 0.246$ nm is the lattice constant. The lattice vectors of layer l after the rotation are given by $\mathbf{a}_i^{(l)} = R(\mp\theta/2)\mathbf{a}_i$ with $\mp$ for $l = 1,2$, respectively, where $R(\theta)$ represents the rotation by θ.

When $\boldsymbol{\delta}$ is fixed to 0, the rotations $\theta = 0$ and 60° give AA and AB stacking, respectively. $60^\circ - \theta$ is equivalent to $-\theta$ followed by a relative translation of layer 2 from site A to site B.[48,49] Also, θ and $-\theta$ are mirror images sharing equivalent band structures. Therefore, it is reasonable to characterize the geometry of TBG by the combination of θ $(0 \leqslant \theta \leqslant 30^\circ)$ and $\boldsymbol{\delta}$.

The lattice structure of TBG is not periodic in general angles because the periods of two graphene layers are generally incommensurate with each layer. But in some special angles where two periods happen to match, the structure becomes rigorously periodic, giving a finite unit cell. This takes place when θ coincides with the angle between $\mathbf{v}_1 = m\mathbf{a}_1 + n\mathbf{a}_2$ and $\mathbf{v}_2 = n\mathbf{a}_1 + m\mathbf{a}_2$ with certain integers m and n, because

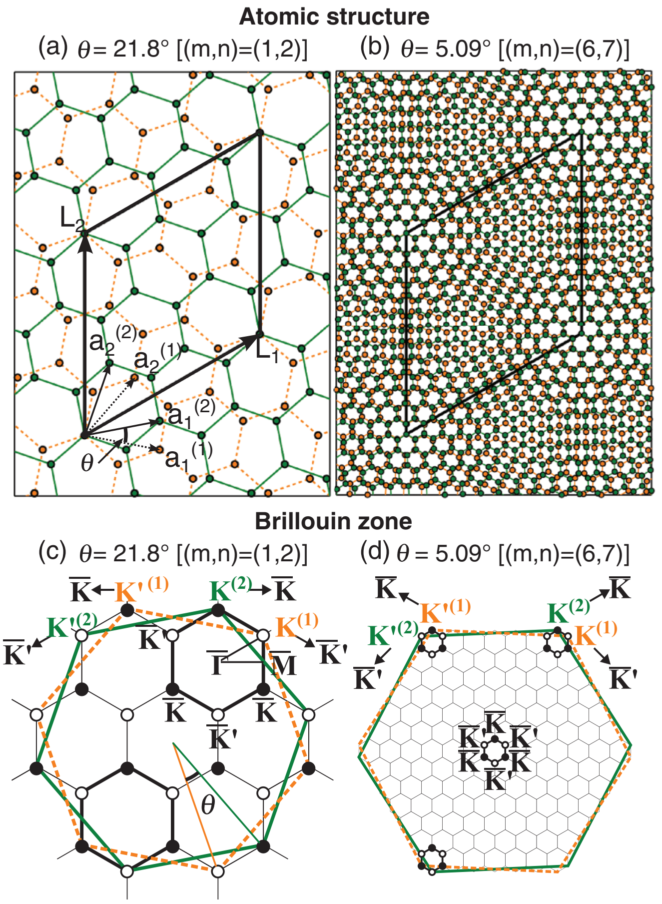

FIG. 1. (Color online) Atomic structures of TBGs with (a) $\theta = 21.8^\circ$ and (b) $\theta = 5.09^\circ$. Dashed (orange) and solid (green) lines represent the lattices of layers 1 and 2, respectively. Brillouin zone of TBGs with (c) $\theta = 21.8^\circ$ and (d) $\theta = 5.09^\circ$. Dashed (orange) and solid (green) large hexagons indicate the first Brillouin zone of layers 1 and 2, respectively, and the thick small hexagon is the folded Brillouin zone of TBG.

then the lattice points $\mathbf{v}_1$ on layer 1 and $\mathbf{v}_2$ on layer 2 of the nonrotated bilayer graphene merge after the rotations $\theta/2$ and $-\theta/2$, respectively. The lattice vectors of the superlattice unit cell are thus given by[48]

$$\mathbf{L}_1 = m\mathbf{a}_1^{(1)} + n\mathbf{a}_2^{(1)} = n\mathbf{a}_1^{(2)} + m\mathbf{a}_2^{(2)} \tag{1}$$

and $\mathbf{L}_2 = R(\pi/3)\mathbf{L}_1$. The rotation angle θ is related to (m,n) by

$$\cos\theta = \frac{1}{2}\frac{m^2+n^2+4mn}{m^2+n^2+mn}. \tag{2}$$

The lattice constant $L = |\mathbf{L}_1| = |\mathbf{L}_2|$ is

$$L = a\sqrt{m^2+n^2+mn} = \frac{|m-n|a}{2\sin(\theta/2)}. \tag{3}$$

Figures 1(a) and 1(b) show the atomic structures of TBG with two rotation angles, $\theta = 21.8^\circ$ $[(m,n) = (1,2)]$ and 5.09° $[(m,n) = (6,7)]$, respectively. We assume $\boldsymbol{\delta} = 0$ unless otherwise noted, and we discuss the effect of $\boldsymbol{\delta} \neq 0$ in Sec. III C. Figures 1(c) and 1(d) show the corresponding Brillouin zone in the extended scheme. In each figure, the dashed (orange) and solid (green) large hexagons correspond to the first Brillouin zones of layers 1 and 2, respectively, and the thick small hexagon to the folded Brillouin zone of TBG. $K^{(l)}$ and $K'^{(l)}$ denote the two inequivalent valleys of layer l. The four valleys $K^{(1)}$, $K'^{(1)}$, $K^{(2)}$, and $K'^{(2)}$ of the two layers are folded back to the two Dirac points, $\bar{K}$ and $\bar{K}'$, in the folded Brillouin zone.[13]

When the rotation angle is small, the mismatch between the lattice vectors of the two layers gives rise to a Moiré pattern with a long spatial period as shown in Fig. 1(b).[13,50] The local lattice structure near a certain point $\mathbf{r}$ approximates a nonrotated bilayer graphene with displacement $\boldsymbol{\delta}$, which depends on the position as

$$\boldsymbol{\delta}(\mathbf{r}) = 2\sin(\theta/2)(\mathbf{e}_z \times \mathbf{r}), \tag{4}$$

where $\mathbf{r}$ is measured from the center of the rotation, and $\mathbf{e}_z$ is a unit vector perpendicular to the plane. The period of the Moiré pattern $\mathbf{L}_i^{\mathrm{M}}$ can be obtained by the condition that $\boldsymbol{\delta}(\mathbf{L}_i^{\mathrm{M}})$ coincides with a primitive lattice vector of the original AA-stacked bilayer. We may choose

$$\mathbf{L}_1^{\mathrm{M}} = \frac{(-\mathbf{a}_1 + \mathbf{a}_2)\times\mathbf{e}_z}{2\sin(\theta/2)}, \quad \mathbf{L}_2^{\mathrm{M}} = \frac{-\mathbf{a}_1 \times \mathbf{e}_z}{2\sin(\theta/2)}, \tag{5}$$

giving $\boldsymbol{\delta}(\mathbf{L}_1^{\mathrm{M}}) = -\mathbf{a}_1 + \mathbf{a}_2$ and $\boldsymbol{\delta}(\mathbf{L}_2^{\mathrm{M}}) = -\mathbf{a}_1$. The lattice constant $L_{\mathrm{M}} = |\mathbf{L}_1^{\mathrm{M}}| = |\mathbf{L}_2^{\mathrm{M}}|$ is

$$L_{\mathrm{M}} = \frac{a}{2\sin(\theta/2)}. \tag{6}$$

The Moiré superlattice vectors $\mathbf{L}_i^{\mathrm{M}}$ can always be defined for any θ, even when the lattice structure is incommensurate. At commensurate angles, the rigorous superlattice period L is exactly $|m-n|$ times bigger than the Moiré period L_{M}. In Fig. 2, we illustrate the lattice structures of $\theta = 13.2^\circ$ $[(m,n) = (2,3)]$, $\theta = 11.0^\circ$ $[(m,n) = (5,7)]$, and $\theta = 9.43^\circ$ $[(m,n) = (3,4)]$. We can see that the atomic structure exactly matches the Moiré pattern in 13.2° and $9.43^\circ (|m-n| = 1)$, while in 11.0°, the exact period L is twice as large as L_{M} since $|m-n| = 2$, and accordingly the atomic structure is slightly different between neighboring units in the Moiré pattern.

B. Tight-binding model

We calculate the eigenenergies and eigenfunctions in TBG using the tight-binding model for p_z atomic orbitals. The Hamiltonian is written as

$$H = -\sum_{\langle i,j\rangle} t(\mathbf{R}_i - \mathbf{R}_j)|\mathbf{R}_i\rangle\langle\mathbf{R}_j| + \mathrm{H.c.}, \tag{7}$$

where $\mathbf{R}_i$ and $|\mathbf{R}_i\rangle$ represent the lattice point and the atomic state at site i, respectively, and $t(\mathbf{R}_i - \mathbf{R}_j)$ is the transfer integral between site i and site j. We adopt an approximation,[14,51–53]

$$\begin{aligned} -t(\mathbf{d}) &= V_{pp\pi}\left[1 - \left(\frac{\mathbf{d}\cdot\mathbf{e}_z}{d}\right)^2\right] + V_{pp\sigma}\left(\frac{\mathbf{d}\cdot\mathbf{e}_z}{d}\right)^2, \\ V_{pp\pi} &= V_{pp\pi}^0 \exp\left(-\frac{d-a_0}{\delta_0}\right), \\ V_{pp\sigma} &= V_{pp\sigma}^0 \exp\left(-\frac{d-d_0}{\delta_0}\right), \end{aligned} \tag{8}$$

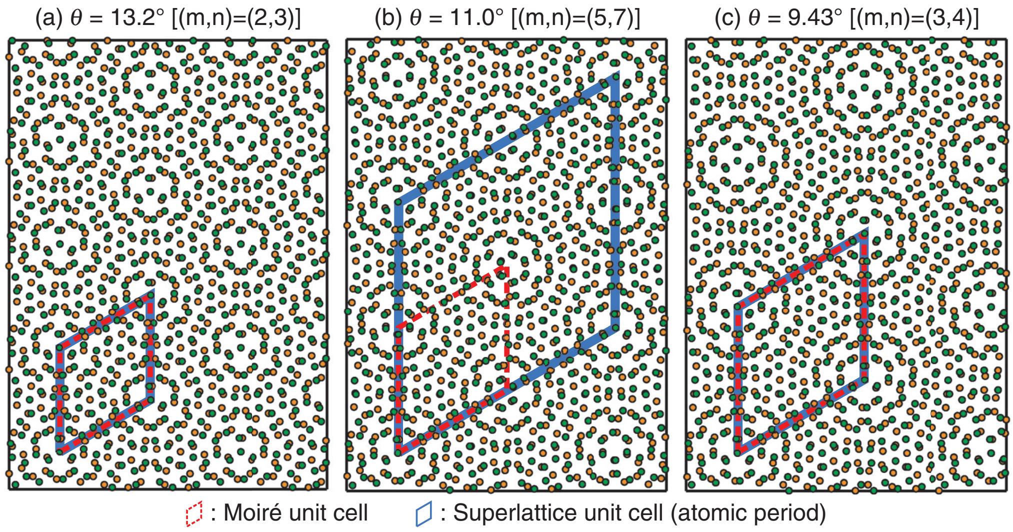

FIG. 2. (Color online) Atomic structures of TBGs with (a) $\theta = 13.2^\circ$, (b) $\theta = 11.0^\circ$, and (c) $\theta = 9.43^\circ$. Dashed (red) and solid (blue) parallelograms correspond to the Moiré unit cell and rigorous superlattice unit cell, respectively.

where $a_0 = a/\sqrt{3} \approx 0.142$ nm is the distance of the neighboring A and B sites on the monolayer, and $d_0 \approx 0.335$ nm is the interlayer spacing. $V^0_{pp\pi}$ is the transfer integral between the nearest-neighbor atoms of monolayer graphene and $V^0_{pp\sigma}$ is that between vertically located atoms on the neighboring layers. Here we take $V^0_{pp\pi} \approx -2.7$ eV and $V^0_{pp\sigma} \approx 0.48$ eV to fit the dispersions of monolayer graphene and AB-stacked bilayer graphene.[14] δ_0 is the decay length of the transfer integral and is chosen as $0.184a$ so that the next-nearest intralayer coupling becomes $0.1 V^0_{pp\pi}$.[14,52] The transfer integral for $d > 4a_0$ is exponentially small and can be safely neglected.

C. Effective continuum model

When the rotation angle is small and the Moiré superlattice period is much larger than the lattice constant, the interaction between the two graphene layers has only the long-wavelength components, allowing one to treat the problem in the effective continuum model. The continuum approaches for TBG have been introduced in several articles.[11,15,16,54] Here we develop a general treatment to construct an effective model directly from the tight-binding Hamiltonian in Eq. (7). To construct the Hamiltonian matrix, we define the Bloch wave basis of a single layer as

$$
\begin{aligned}
|\mathbf{k}, A_l\rangle &= \frac{1}{\sqrt{N}} \sum_{\mathbf{R}_{A_l}} e^{i\mathbf{k}\cdot\mathbf{R}_{A_l}} |\mathbf{R}_{A_l}\rangle, \\
|\mathbf{k}, B_l\rangle &= \frac{1}{\sqrt{N}} \sum_{\mathbf{R}_{B_l}} e^{i\mathbf{k}\cdot\mathbf{R}_{B_l}} |\mathbf{R}_{B_l}\rangle,
\end{aligned}
\tag{9}
$$

where the position $\mathbf{R}_{A_l}(\mathbf{R}_{B_l})$ runs over all $A(B)$ sites in the layer $l(=1,2)$, N is the number of monolayer unit cells in the whole system, and $\mathbf{k}$ is the two-dimensional Bloch wave vector defined in the first Brillouin zone of the monolayer on layer l.

The intralayer matrix element of each layer occurs only within the same wave vector, and it is given by

$$
\begin{aligned}
h_{A_lA_l}(\mathbf{k}) &\equiv \langle \mathbf{k}, A_l | H | \mathbf{k}, A_l \rangle = h(\mathbf{k}, 0), \\
h_{A_lB_l}(\mathbf{k}) &\equiv \langle \mathbf{k}, A_l | H | \mathbf{k}, B_l \rangle = h(\mathbf{k}, \boldsymbol{\tau}_1), \\
h_{B_lB_l}(\mathbf{k}) &= h_{A_lA_l}(\mathbf{k}),
\end{aligned}
\tag{10}
$$

where $\boldsymbol{\tau}_1 = (2\mathbf{a}_2 - \mathbf{a}_1)/3$ is a vector connecting site B site to site A, and

$$
\begin{aligned}
h(\mathbf{k}, \boldsymbol{\tau}) = \sum_{n_1,n_2} & -t(n_1\mathbf{a}_1 + n_2\mathbf{a}_2 + \boldsymbol{\tau}) \\
& \times \exp\left[-i\mathbf{k}\cdot(n_1\mathbf{a}_1 + n_2\mathbf{a}_2 + \boldsymbol{\tau})\right].
\end{aligned}
\tag{11}
$$

The low-energy spectrum of the monolayer graphene is approximated by effective Dirac cones centered at K and K' points.[55–59] We take $\mathbf{K} = (2\pi/a)(-2/3, 0)$ and $\mathbf{K}' = (2\pi/a)(2/3, 0)$ as the K points of nonrotated graphene. The K points of layer l are then given by $\mathbf{K}^{(l)} = R(\mp\theta/2)\mathbf{K}$ and $\mathbf{K}'^{(l)} = R(\mp\theta/2)\mathbf{K}'$, with $\mp$ for $l = 1$ and 2, respectively. When $\mathbf{k}$ is close to either K or K' the intralayer matrix element is approximately written as[59]

$$
\begin{aligned}
& h_{A_lB_l}(\mathbf{k}) \\
& \approx \begin{cases}
-\hbar v\left[\left(k_x - K_x^{(l)}\right) - i\left(k_y - K_y^{(l)}\right)\right] e^{-i\eta^{(l)}} & (\mathbf{k} \approx \mathbf{K}), \\
-\hbar v\left[-\left(k_x - K_x'^{(l)}\right) - i\left(k_y - K_y'^{(l)}\right)\right] e^{i\eta^{(l)}} & (\mathbf{k} \approx \mathbf{K}'),
\end{cases}
\end{aligned}
\tag{12}
$$

where $\eta^{(l)} = \pm\theta/2$ for $l = 1$ and 2, respectively. The parameter v is the band velocity of the Dirac cone, which is given in the present tight-binding parametrization as

$$
v \approx \frac{\sqrt{3}}{2}\frac{a}{\hbar} V^0_{pp\pi}\left(1 - 2e^{-a_0/\delta_0}\right),
\tag{13}
$$

where the first and second terms in parentheses originate from the hopping between the first and the second nearest AB pairs, respectively. In the following, we neglect the phase factor $e^{-i\eta^{(l)}}$, assuming $\theta \ll 1$. Indeed, we numerically checked that the neglected phase gives a slight energy shift, of the order of

θ^2 at most. The diagonal matrix element $h_{A_lA_l}(\mathbf{k}) = h_{B_lB_l}(\mathbf{k})$ is shown to be of the order of $|\mathbf{k}-\mathbf{K}|^2$ and $|\mathbf{k}-\mathbf{K}'|^2$ near points K and K', respectively, and is neglected in the following.

For the interlayer coupling, we first consider a nonrotated bilayer graphene with $\theta = 0$ and a fixed lattice displacement $\boldsymbol{\delta}$. The unit cell is spanned by the monolayer lattice vectors, $\mathbf{a}_1$ and $\mathbf{a}_2$, which are now shared by both layers. As the system has the same periodicity as the monolayer, interlayer coupling occurs within states belonging to the same $\mathbf{k}$. The interlayer matrix element is written as

$$\begin{aligned} U_{A_2A_1}(\mathbf{k},\boldsymbol{\delta}) &\equiv \langle \mathbf{k},A_2|H|\mathbf{k},A_1\rangle = u(\mathbf{k},\boldsymbol{\delta}),\\ U_{B_2B_1}(\mathbf{k},\boldsymbol{\delta}) &\equiv \langle \mathbf{k},B_2|H|\mathbf{k},B_1\rangle = u(\mathbf{k},\boldsymbol{\delta}),\\ U_{B_2A_1}(\mathbf{k},\boldsymbol{\delta}) &\equiv \langle \mathbf{k},B_2|H|\mathbf{k},A_1\rangle = u(\mathbf{k},\boldsymbol{\delta}-\boldsymbol{\tau}_1),\\ U_{A_2B_1}(\mathbf{k},\boldsymbol{\delta}) &\equiv \langle \mathbf{k},A_2|H|\mathbf{k},B_1\rangle = u(\mathbf{k},\boldsymbol{\delta}+\boldsymbol{\tau}_1), \end{aligned} \tag{14}$$

where

$$\begin{aligned} u(\mathbf{k},\boldsymbol{\delta}) = &\sum_{n_1,n_2} -t(n_1\mathbf{a}_1 + n_2\mathbf{a}_2 + d_0\mathbf{e}_z + \boldsymbol{\delta})\\ &\times \exp\left[-i\mathbf{k}\cdot(n_1\mathbf{a}_1 + n_2\mathbf{a}_2 + \boldsymbol{\delta})\right] \end{aligned} \tag{15}$$

$u(\mathbf{k},\boldsymbol{\delta})$ can be immediately calculated by taking a summation over some small n_i's, since $t(\mathbf{d})$ rapidly vanishes in $|\mathbf{d}| \gg a$.

When θ is slightly shifted from 0 to a small finite angle, the local lattice structure is approximately viewed as a nonrotated bilayer graphene, where the displacement $\boldsymbol{\delta}$ is slowly varying in space in accordance with Eq. (4). Then the interlayer interaction couples wave vectors $\mathbf{k}$ and $\mathbf{k}'$, which are close to each other such that $|\mathbf{k}'-\mathbf{k}| \ll 2\pi/a$. The interlayer matrix element is approximately written as

$$\begin{aligned} &\langle \mathbf{k}',X_2'|H|\mathbf{k},X_1\rangle\\ &\approx \frac{1}{\Omega_\mathrm{M}}\int_{\Omega_\mathrm{M}} d\mathbf{r}\, U_{X_2'X_1}\left[\frac{\mathbf{k}+\mathbf{k}'}{2},\boldsymbol{\delta}(\mathbf{r})\right] e^{-i(\mathbf{k}'-\mathbf{k})\cdot\mathbf{r}}, \end{aligned} \tag{16}$$

where X and X' are of either A or B, $U_{X_2'X_1}$ are the interlayer coupling in the nonrotational bilayer in Eq. (14), and $\Omega_\mathrm{M} = |\mathbf{L}_1^\mathrm{M} \times \mathbf{L}_2^\mathrm{M}|$ is the Moiré superlattice unit cell. The derivation of Eq. (16) is detailed in the Appendix. $U_{X_2'X_1}[\mathbf{q},\boldsymbol{\delta}(\mathbf{r})]$ is periodic in $\mathbf{r}$ with the Moiré superlattice periods, and therefore the matrix element, Eq. (16), is nonzero only when $\mathbf{k}'-\mathbf{k} = n_1\mathbf{G}_1^\mathrm{M} + n_2\mathbf{G}_2^\mathrm{M}$, where $\mathbf{G}_i^\mathrm{M}$ is the reciprocal lattice vector satisfying $\mathbf{L}_i^\mathrm{M}\cdot\mathbf{G}_j^\mathrm{M} = 2\pi\delta_{ij}$, and n_i is an integer.

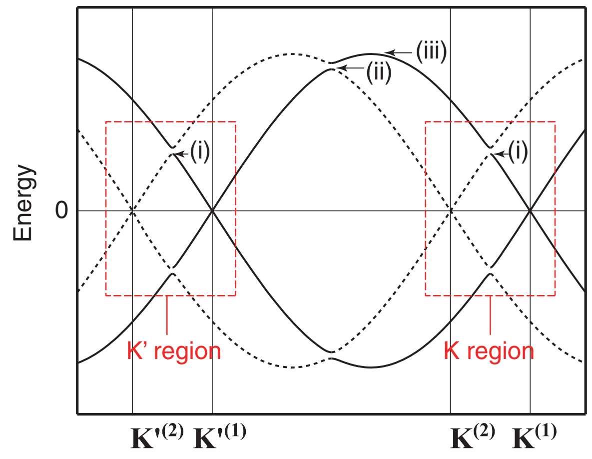

FIG. 3. (Color online) Schematic band structures of TBG in the extended zone scheme along the line $K'^{(2)}$-$K'^{(1)}$-$K^{(2)}$-$K^{(1)}$. (i), (ii) and (iii) indicate the saddle points.

In TBG, the low-energy physics is still dominated by the states near points K and K' because the interlayer coupling is much smaller than intralayer coupling. Besides, the states near K and those near K' are far apart in the wave space when θ is small, so that they are not hybridized by the interlayer coupling. Therefore, we may consider two valleys separately in constructing the Hamiltonian, and the factor $(\mathbf{k}+\mathbf{k}')/2$ in Eq. (16) can be replaced with $\mathbf{K}$ or $\mathbf{K}'$. In the real-space representation, the effective Hamiltonian near K is concisely written in the basis of $\{|A_1\rangle,|B_1\rangle,|A_2\rangle,|B_2\rangle\}$ as

$$H_\mathrm{eff} = \begin{pmatrix} H_1 & U^\dagger \\ U & H_2 \end{pmatrix}, \tag{17}$$

with

$$\begin{aligned} H_l &= -\hbar v(\hat{\mathbf{k}} - \Delta\mathbf{K}^{(l)})\cdot\boldsymbol{\sigma},\\ U &= \begin{pmatrix} u(\mathbf{K},\boldsymbol{\delta}) & u(\mathbf{K},\boldsymbol{\delta}+\boldsymbol{\tau}_1) \\ u(\mathbf{K},\boldsymbol{\delta}-\boldsymbol{\tau}_1) & u(\mathbf{K},\boldsymbol{\delta}) \end{pmatrix}, \end{aligned} \tag{18}$$

where $\hat{\mathbf{k}} = -i\partial/\partial\mathbf{r}$, $\boldsymbol{\sigma} = (\sigma_x,\sigma_y)$ is the Pauli matrices, $\Delta\mathbf{K}^{(l)} = \mathbf{K}^{(l)} - \mathbf{K}$, and $\boldsymbol{\delta} = \boldsymbol{\delta}(\mathbf{r})$ is defined in Eq. (4). When deriving H_l in Eq. (18) from Eq. (12), we replace $\mathbf{k}$ with $\hat{\mathbf{k}} + \mathbf{K}$, i.e., measure the wave number relative to the common point $\mathbf{K}$ for both layers. The Hamiltonian for K' is obtained by replacing $\mathbf{K}$ with $\mathbf{K}'$ and $\hat{k}_x$ with $-\hat{k}_x$ above. In the present choice of the tight-binding parameters $V_{pp\pi}^0$, $V_{pp\sigma}^0$, and δ_0, the effective interlayer coupling $u(\mathbf{K},\boldsymbol{\delta}(\mathbf{r}))$ is approximately written in terms of only a few Fourier components as

$$u(\mathbf{K},\boldsymbol{\delta}(\mathbf{r})) \approx (0.103\ \mathrm{eV}) \times \left[1 + e^{-i\mathbf{G}_2^\mathrm{M}\cdot\mathbf{r}} + e^{-i(\mathbf{G}_1^\mathrm{M}+\mathbf{G}_2^\mathrm{M})\cdot\mathbf{r}}\right], \tag{19}$$

where $u(\mathbf{K}',\boldsymbol{\delta})$ is given by $u(\mathbf{K},\boldsymbol{\delta})^*$. The expression of $u(\mathbf{K},\boldsymbol{\delta})$ explicitly depends on the choice of the $\mathbf{K}$ vector out of three equivalent corners in the Brillouin zone.

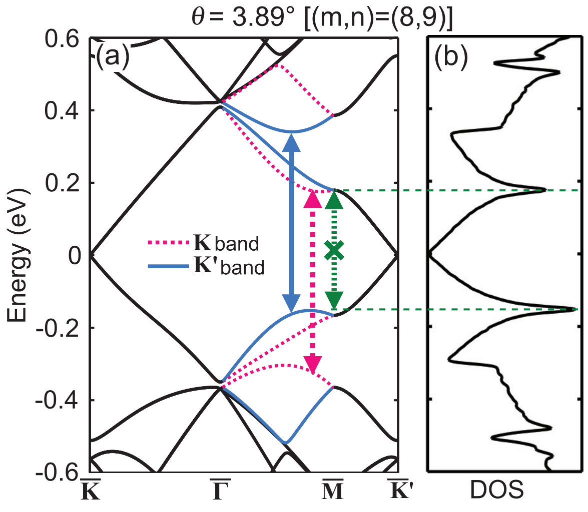

FIG. 4. (Color online) (a) Band structure and (b) density of states of TBG with $\theta = 3.89°$. Solid (blue) and dashed (pink) arrows represent the excitation corresponding to the major peaks in the optical absorption, and the dotted (green) arrow is a process optically forbidden (see text).

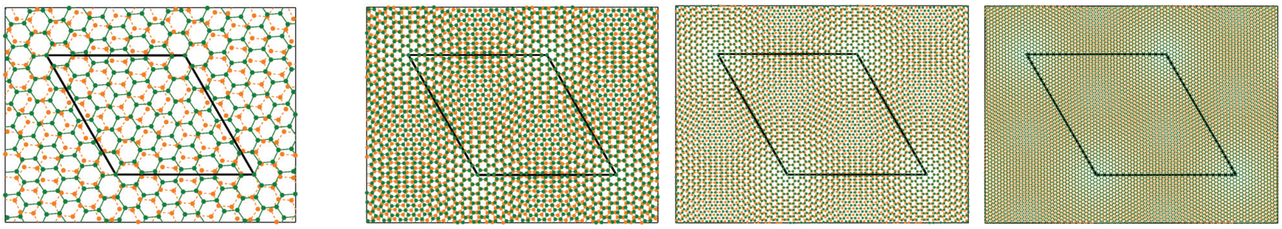

(a) θ = 9.43° [(m,n)=(3,4)] (b) θ = 3.89° [(m,n)=(8,9)] (c) θ = 2.65° [(m,n)=(12,13)] (d) θ = 1.47° [(m,n)=(22,23)]

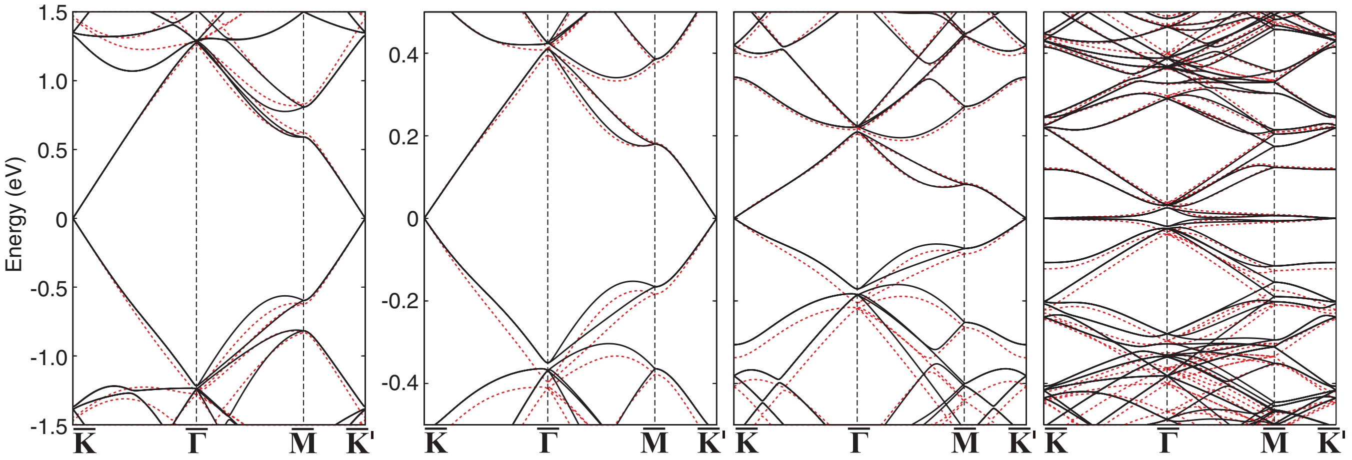

FIG. 5. (Color online) Atomic structures (top) and band structures (bottom) of TBGs with (a) $\theta = 9.43^\circ$, (b) $\theta = 3.89^\circ$, (c) $\theta = 2.65^\circ$, and (d) $\theta = 1.47^\circ$, calculated by the tight-binding model [solid (black) lines] and the effective continuum model [dashed (red) lines]. The Dirac point energy is set to 0.

In the k-space representation, the Hamiltonian matrix can be written in the space of the single-layer bases at discrete k points $\mathbf{k} = \mathbf{k}_0 + n_1\mathbf{G}_1^{\rm M} + n_2\mathbf{G}_2^{\rm M}$, where $\mathbf{k}_0$ is a vector defined in the superlattice Brillouin zone spanned by $\mathbf{G}_1^{\rm M}$ and $\mathbf{G}_2^{\rm M}$. $\mathbf{k}_0 = 0$ corresponds to the $\bar{M}$ point. To obtain the energy spectrum and eigen–wave function, we choose k points satisfying $\hbar v|\mathbf{k}| \lesssim E_{\rm max}$ with a sufficiently large $E_{\rm max}$ and diagonalize the Hamiltonian within the limited wave space. To avoid a discrete change in the number of bases in varying $\mathbf{k}_0$, we adopt a soft cutoff which gradually reduces the matrix elements for the single-layer bases beyond $E_{\rm max}$.

It is straightforward to show that the Hamiltonian, Eq. (17), has a certain symmetry expressed as

$$\hat{\Sigma}^{-1} H_{\rm eff} \hat{\Sigma} = -H^*_{\rm eff}, \tag{20}$$

where

$$\hat{\Sigma} = \begin{pmatrix} 0 & \sigma_x \\ -\sigma_x & 0 \end{pmatrix}. \tag{21}$$

This immediately demonstrates that if ψ is an eigenstate of $H_{\rm eff}$ belonging to energy E, $\hat{\Sigma}\psi^*$ is an eigenstate of energy $-E$.

D. Dynamical conductivity

Using the eigen–wave functions obtained by the tight-binding model or the effective continuum model, we calculate the dynamical conductivity

$$\sigma_{xx}(\omega) = \frac{e^2\hbar}{iS}\sum_{\alpha,\beta}\frac{f(\varepsilon_\alpha)-f(\varepsilon_\beta)}{\varepsilon_\alpha-\varepsilon_\beta}\frac{|\langle\alpha|v_x|\beta\rangle|^2}{\varepsilon_\alpha-\varepsilon_\beta+\hbar\omega+i\eta}, \tag{22}$$

where the sum is over all states, S is the area of the system, $f(\varepsilon)$ is the Fermi distribution function, ε_α (ε_β) and $|\alpha\rangle$ ($|\beta\rangle$) represent the eigenenergy and the eigenstate of the system, $v_x = -(i/\hbar)[x,H]$ is the velocity operator, and η is the phenomenological broadening, which is set to 3 meV in the following calculations. The optical absorption intensity at photon energies $\hbar\omega$ is related to the real part of $\sigma(\omega)$. The transmission of incident light perpendicular to a two-dimensional system is given by[60]

$$T = \left|1 + \frac{2\pi}{c}\sigma_{xx}(\omega)\right|^{-2} \approx 1 - \frac{4\pi}{c}\mathrm{Re}\,\sigma_{xx}(\omega). \tag{23}$$

III. RESULTS AND DISCUSSION

A. Band structure

The band dispersion of TBG can be intuitively understood in terms of coupled four Dirac cones centered at the valleys $K^{(l)}$ and $K'^{(l)}$ ($l = 1,2$). Figure 3 shows the schematic band structures of TBG along the line $K'^{(2)}$-$K'^{(1)}$-$K^{(2)}$-$K^{(1)}$ in the extended zone scheme. Here dashed and solid dispersions represent the energy bands of layers 1 and 2, respectively. The interlayer coupling gives rise to band anticrossing at the intersection, and the resultant energy band is characterized by saddle points accompanied by the van Hove singularity in the

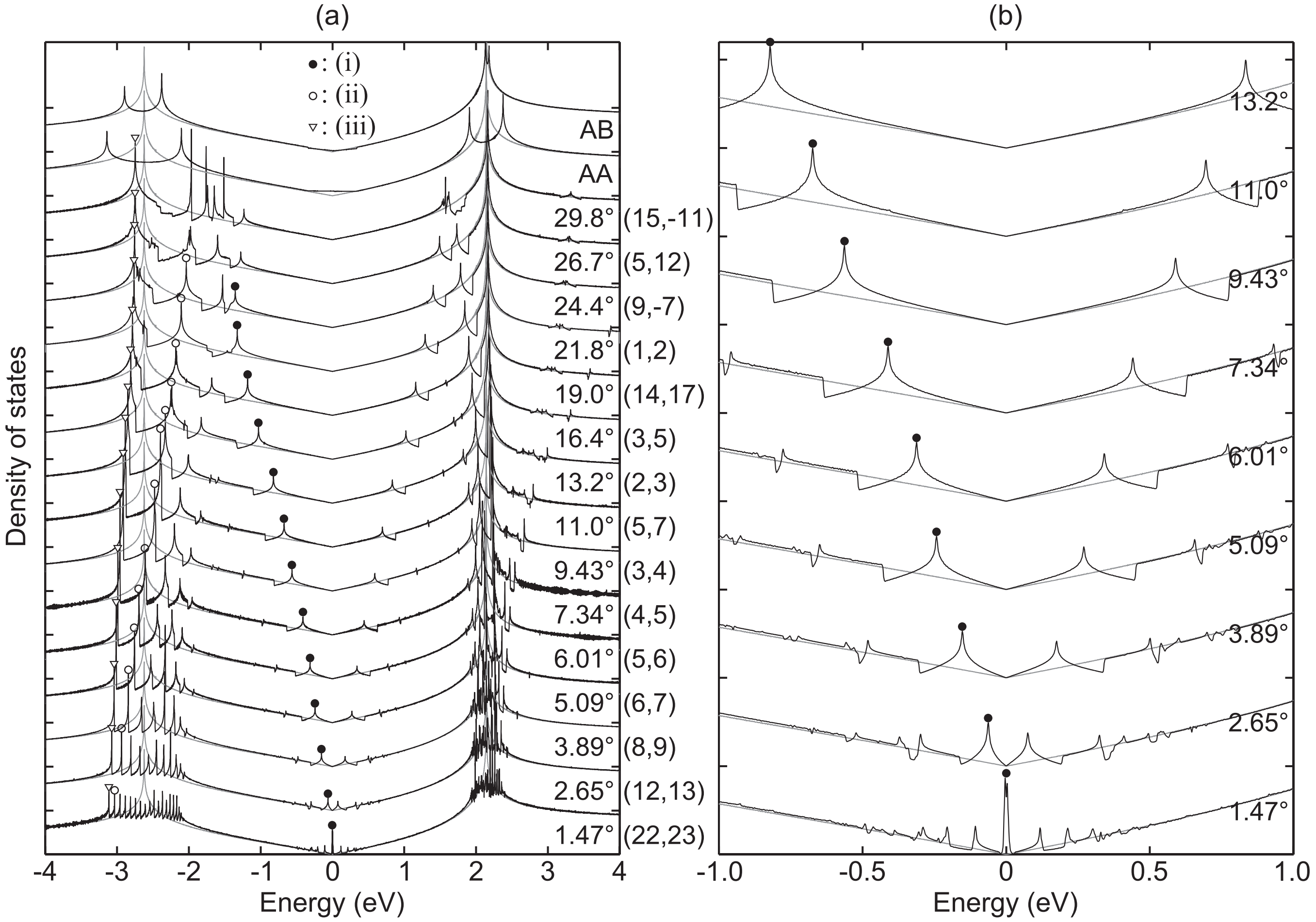

FIG. 6. DOS of TBGs with various rotation angles $0^\circ < \theta < 30^\circ$ in (a) wide and (b) narrow ranges of energy. The DOS of uncoupled bilayer graphene (i.e., twice the monolayer's DOS) is shown as light-gray lines. Peaks marked with symbols correspond to three different types of van Hove singularity (see text).

density of states (DOS). The saddle points are classified as (i), (ii), and (iii) as shown in Fig. 3, where (i) and (ii) result from the band intersection of different layers, while (iii) originates from the original monolayer's band structure. In the limit $\theta \to 0$, $K^{(1)}$ and $K^{(2)}$ (equivalently, $K'^{(1)}$ and $K'^{(2)}$) get closer, so that (i) approaches the Dirac points, while (ii) goes to the midpoint between K and K' in the high-energy region. (iii) remains at the constant energy.

Figures 4(a) and 4(b) show the band structure and the DOS, respectively, of TBG with $\theta = 3.89^\circ$ $[(m,n) = (8,9)]$ actually calculated by the tight-binding model, Eq. (7). The band structure can be viewed as the monolayer's Dirac cone folded into the superlattice Brillouin zone with some band anticrossing at the zone corner.[7,11,12,61–64] The lowest band exhibits a linear dispersion near $\bar{K}$ and $\bar{K}'$, while we see a large splitting in energy near point $\bar{M}$, from ±0.2 to ±0.4 eV, respectively, corresponding to band anticrossing (i) in Fig. 3.[8,64,65] The DOS has a sharp peak around ±0.2 eV, which is associated with the saddle point near point $\bar{M}$.

Each energy band can be classified into either those originating from the monolayer's K region (i.e., $K^{(1)}$ and $K^{(2)}$) or those from the K' region (i.e., $K'^{(1)}$ and $K'^{(2)}$), because two valleys are hardly mixed by the interlayer interaction with this small rotation angle. Here K and K' should not be confused with $\bar{K}$ and $\bar{K}'$ for the folded Brillouin zone. The monolayer's band near K and that near K' are independently folded into the same Brillouin zone without mixing with each other. Indeed, the lowest band in Fig. 4(a) is composed of nearly degenerate branches, where dashed (pink) and solid (blue) lines are the bands from K and K', respectively. These two bands are degenerate along $\bar{K}$-$\bar{\Gamma}$ and $\bar{M}$-$\bar{K}'$, reflecting the C_2 symmetry in the real-space lattice structure.[64]

Figure 5 shows the energy bands of TBGs with different rotation angles, from $\theta = 9.43^\circ$ down to $\theta = 1.47^\circ$. The structures are similar to each other, while the overall energy scale shrinks as the rotation angle decreases, roughly in proportion to the size of the folded Brillouin zone. The width of splitting at the $\bar{M}$ point is about 0.2 eV in every case, which is of the order of the interlayer coupling $V^0_{pp\sigma}$. In TBGs with small rotation angles, less than 2°, the energy scale of the folded Dirac cone becomes comparable to the band splitting so that the band velocity near the Dirac cone is significantly reduced from the monolayer's.[2,7,11–16] In Fig. 5, we also plot the band energies calculated by the effective continuum model, Eq. (17),

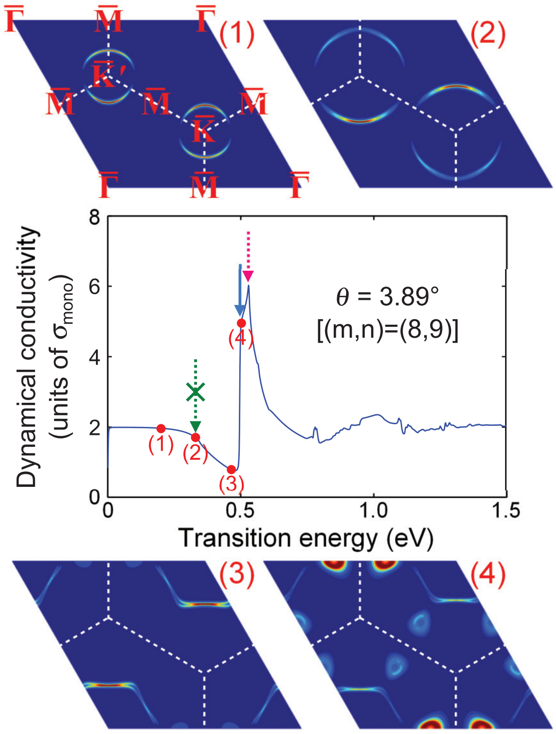

FIG. 7. (Color online) Middle: Dynamical conductivity of TBG with $\theta = 3.89^\circ$ as a function of the transition energy. Arrows indicate the excitation energies of the transitions shown in Fig. 4(a). Top and bottom: Spectral weight maps in the superlattice Brillouin zone at several transition energies.

as dashed (red) lines, to be compared with the solid (black) curves obtained by the original tight-binding model. We see that the low-energy band structure agrees quite well, except that the effective model fails to reproduce a small electron-hole asymmetry in the original model, since it assumes a symmetric Dirac cone for the intralayer Hamiltonian.

Figure 6 shows the DOS of TBGs with various rotation angles $0^\circ < \theta < 30^\circ$ with wide [Fig. 6(a)] and narrow [Fig. 6(b)] energy ranges. To each curve, we append the DOS of uncoupled bilayer graphene (i.e., twice the monolayer's) as a light-gray line. We observe a number of characteristic peaks associated with van Hove singularities (i), (ii), and (iii) argued in Fig. 3. As the rotation angle increases, peaks (i) move away from the Dirac points, and peaks (ii) move towards the Dirac points, while peaks (iii) stay at an almost-constant energy. In TBGs with small rotation angles, we see a number of additional peaks since the interlayer coupling of higher order in the Moiré wave number becomes significant.

B. Optical absorption

In Fig. 7, we plot the dynamical conductivity of TBG with $\theta = 3.89^\circ$ calculated with the tight-binding model. The conductivity is plotted in units of

$$\sigma_{\text{mono}} = \frac{g_v g_s}{16}\frac{e^2}{\hbar}, \tag{24}$$

which is the universal dynamical conductivity of monolayer graphene under a linear band regime, where $g_s = 2$ and $g_v = 2$ are the spin and valley (K, K') degeneracy, respectively.[24,36–39] The spectrum is characterized by a peak around 0.5 eV and a considerable reduction right below the peak energy. Otherwise the conductivity is close to $2\sigma_{\text{mono}}$. The top and bottom panels, numbered from (1) to (4), show spectral weight maps at specific photon energies, which highlight the wave vectors that contribute to the optical transition. A sudden rise in the conductivity between (3) and (4) is due to bright spots near point $\bar{M}$ in the weight map. This actually corresponds to the transition from the saddle point in the lowest valence band to the second conduction band, which is marked by a solid (blue) arrow in the band diagram in Fig. 4(a). The similar transition indicated by the dashed (pink) arrow occurs at a slightly higher energy due to the electron-hole asymmetry. Below the peak energy, the dynamical conductivity is significantly reduced and becomes lower than $2\sigma_{\text{mono}}$, because the number of available states largely decreases due to the band anticrossing.

It should be noted that the transition does not occur between the saddle points of the lowest conduction and valence bands [dotted (green) arrow in Fig. 4(a)], because it is optically forbidden in this particular system. This can be clearly explained by the effective continuum model as follows. The lowest electron and hole states at point $\bar{M}$, which are connected by the dotted arrow in Fig. 4, are an electron-hole pair related by the symmetry of Eq. (20), and thus these wave functions are written as ψ and $\hat{\Sigma}\psi^*$. The matrix element of v_x between the two states is obviously 0, because

$$\begin{aligned}\langle \hat{\Sigma}\psi^* | v_x | \psi \rangle &= \begin{pmatrix} \psi_4^* \\ \psi_3^* \\ -\psi_2^* \\ -\psi_1^* \end{pmatrix}^\dagger \begin{pmatrix} v\sigma_x & 0 \\ 0 & v\sigma_x \end{pmatrix} \begin{pmatrix} \psi_1 \\ \psi_2 \\ \psi_3 \\ \psi_4 \end{pmatrix} \\ &= v(\psi_4\psi_2 + \psi_3\psi_1 - \psi_2\psi_4 - \psi_1\psi_3) = 0,\end{aligned} \tag{25}$$

and thus the transition is optically inactive. This symmetry does not limit the optical selection rule at points other than $\bar{M}$ [the origin of the wave number in the effective Hamiltonian, Eq. (17)], since ψ and $\hat{\Sigma}\psi^*$ generally reside at different Bloch wave vectors and are not connected by the optical transition.

In Fig. 8(a), we plot the optical absorption spectra at various rotation angles in a wide frequency range. The spectrum exhibits characteristic conductivity peaks ranging from terahertz to ultraviolet frequencies. The peaks are again classified into three groups similarly to the DOS. When the rotation angle increases from 0° to 30°, peak (i) [(ii)] moves to higher (lower) energies, while peak (iii) remains unchanged. Figure 8(b) shows magnified plots of the low-frequency range for several small angles. There the spectrum is characterized by a single peak belonging to group (i), similarly to Fig. 7, and its transition energy monotonically shifts with the rotation angle. In $\theta = 1.47^\circ$, the spectrum exhibits a complicated structure in accordance with the strong band deformation observed in Fig. 5. In Fig. 8(b), we also present the spectrum of the effective continuum model as dashed (red) curves, to be compared with the original tight-binding calculation. The results agree quite well except for the peak splitting due to the electron-hole asymmetry, which is pronounced in $\theta \gtrsim 10^\circ$.

As argued in Sec. II A, the rigorous superlattice period L in Eq. (3) discontinuously changes, depending on the commensurability of the lattice periods. Nevertheless, the DOS in Fig. 6 and the optical absorption spectrum in Fig. 8 show that the peak structure almost continuously evolves with the rotation angle, suggesting that the exact lattice commensurability is not quite important for the physical property. Although we cannot rigorously handle incommensurate TBGs due to the infinite unit cell size, its optical spectrum should be approximated by interpolating those of commensurate TBGs with similar rotation angles. The only property in which the actual lattice period L matters is found as tiny peaks in the conductivity indicated as dashed (blue) circles in Fig. 8, which exist only when $|m-n| > 1$. They are related to the transition at the corner of the exact superlattice Brillouin zone.

It is interesting to ask what the optical spectrum looks like in the limit of vanishing rotation angle θ. When θ is small but finite, the local lattice structure is approximately viewed as a nonrotated bilayer graphene with a certain lattice displacement $\boldsymbol{\delta}$, which is slowly varying in space; i.e., the system includes AA, AB, or any intermediate structures within a long spatial period. Since the system can then be regarded as an ensemble of nonrotated bilayers with all possible $\boldsymbol{\delta}$'s, we expect that the absorption spectrum approaches its average over $\boldsymbol{\delta}$. This should be checked by actually averaging the optical spectra, and it is left for a future study.

C. Effect of lattice displacement

The electronic structure of TBG generally depends on the lattice displacement $\boldsymbol{\delta}$, which was set to 0 in the above calculations. When the superlattice unit cell is of the order of the atomic scale, in particular, the lattice structure depends considerably on $\boldsymbol{\delta}$, and it seems to dramatically influence the band structure and the optical absorption. We have the largest variation when $\theta = 0$, where the lattice constant L coincides with a. There AA stacking is transformed to AB stacking by a translation $\boldsymbol{\delta}$, and indeed the band structure and the optical spectrum are significantly different as shown in Figs. 6 and 8, respectively.

The TBG with $(m,n) = (1,2)$ $(\theta = 21.8^\circ)$ has the next smallest primitive unit cell of $L = \sqrt{7}a$. Here we calculate the optical spectra of the two most distinct cases, $\boldsymbol{\delta} = 0$ and $(\mathbf{a}_1^{(2)} + \mathbf{a}_2^{(2)})/3$, whose atomic structures are displayed in Figs. 9(a) and 9(b), respectively. Figures 9(c) and 9(d) show the electronic structure and the dynamical conductivity, respectively, of the two different TBGs. Even though the atomic structures are still apparently different between the

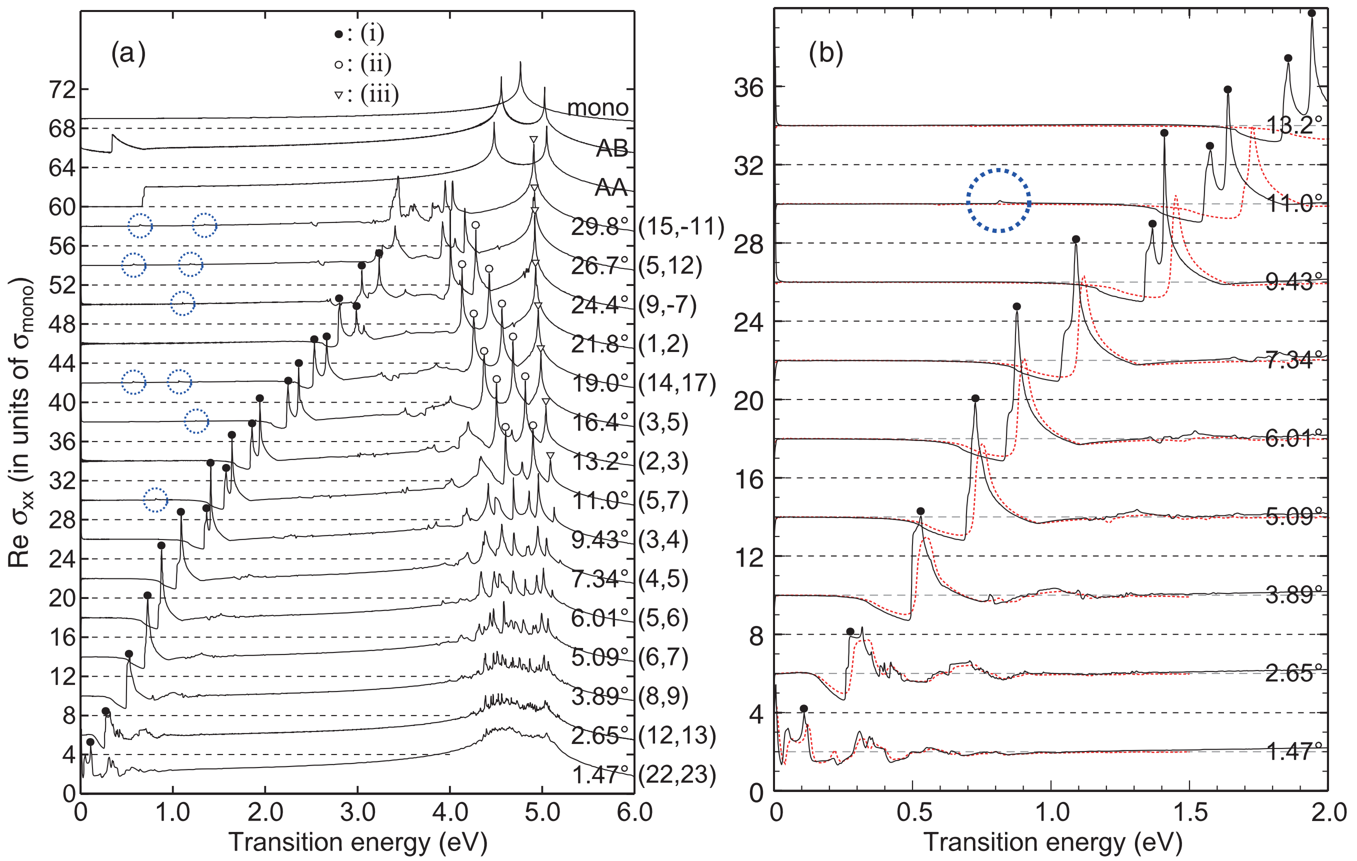

FIG. 8. (Color online) Dynamical conductivities of TBGs with various rotation angles in (a) wide and (b) narrow frequency ranges, calculated by the tight-binding model [solid (black) lines] and the effective continuum model [dashed (red) lines, only for (b)]. Peaks marked with symbols represent the excitations associated with the van Hove singularity in Fig. 6. Dashed (blue) circles indicate the tiny peaks which appearonly when the actual lattice period L is larger than the Moiré period L_{M} (see text).

θ = 21.8° [(m,n)=(1,2)]

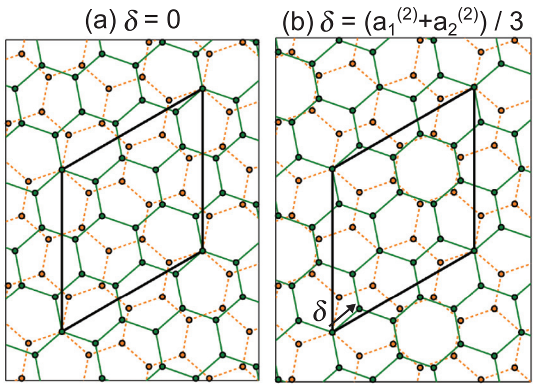

(c) Band structure

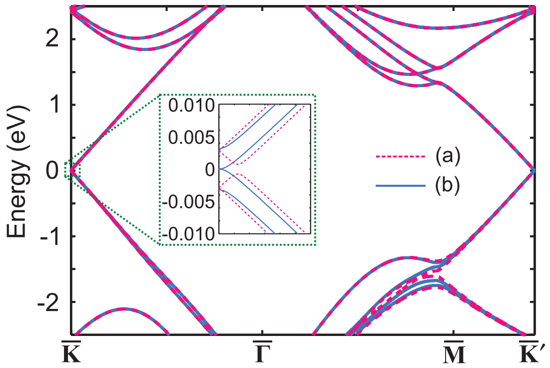

(d) Dynamical conductivity

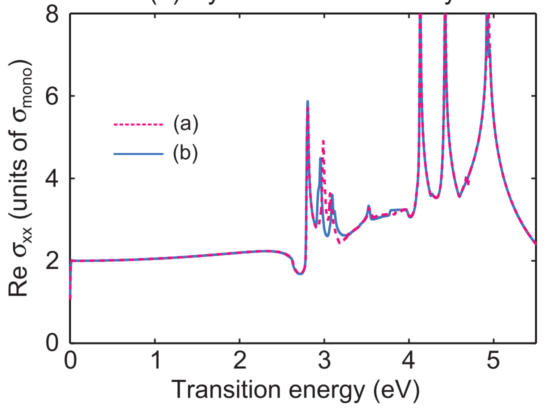

FIG. 9. (Color online) Atomic structures of TBGs with $\theta = 21.8^\circ$ with different translation vectors: (a) $\boldsymbol{\delta} = 0$ and (b) $(\mathbf{a}_1^{(2)} + \mathbf{a}_2^{(2)})/3$. (c) Band structures and (d) dynamical conductivities of the two distinct TBGs.

two, the energy bands are almost equivalent, except that there is a tiny difference near point $\bar{M}$ for which the energy scale is of the order of 10 meV. In the dynamical conductivity, this is reflected in a small difference in the peak structure near the energy of 3 eV. The inset in Fig. 9(c) magnifies the band structure in the vicinity the Dirac points. We observe a small difference of the order of 1 meV, where one takes a form like the *AA* bilayer and the other like the *AB* bilayer,[48,49,62] while it gives no noticeable difference in the dynamical conductivity in Fig. 9(d). The dependence on the lattice displacement becomes even smaller in all other TBGs since their superlattice unit cells are generally larger than that of $\theta = 21.8^\circ$. The variation is completely absent in any incommensurate angles at which the unit cell is infinite. Thus, concerning the energy range of interest, we conclude that the optical spectrum of TBG does not depends much on the lattice displacement, except for $\theta = 0$.

IV. CONCLUSION

We have theoretically investigated the optical absorption properties of TBGs with various stacking geometries using the tight-binding model and the effective continuum model. We have shown that the spectrum is characterized by series of absorption peaks associated with the van Hove singularities in the band structure, and the peak energies systematically shift upon a change in the rotation angle. The optical spectrum almost continuously evolves upon changing the rotation angle, regardless of the rigorous commensurability between two layers, suggesting that the optical absorption measurement provides a convenient way to identify the rotation angle of TBG. We have developed the effective continuum model based on the tight-binding model used here and demonstrated that it well reproduces the low-energy band structure and the dynamical conductivity of the tight-binding model for $\theta < 10^\circ$, and it also explains the optical selection rule analytically in terms of the symmetry of the effective Hamiltonian.

ACKNOWLEDGMENTS

This project was funded by Grant-in-Aid for Research Activity Start-up No. 23840004 (P.M.) and Grant-in-Aid for Scientific Research No. 24740193 (M.K.) from the Japan Society for the Promotion of Science (JSPS) and by JST-EPSRC Japan-UK Cooperative Programme Grant No. EP/H025804/1. P.M. acknowledges the Supercomputer Center, Institute for Solid State Physics, University of Tokyo, for the use of its facilities (Project No. ID: H23-D-0009).

APPENDIX: DERIVATION OF EFFECTIVE INTERLAYER COUPLING

Here we derive the effective interlayer matrix element, Eq. (16), for TBGs with small rotation angles. The matrix element of the Hamiltonian, Eq. (7), between the single-layer bases in the different layers is explicitly written as

$$\begin{aligned}
&\langle \mathbf{k}', X_2' | H | \mathbf{k}, X_1 \rangle \\
&\quad = \frac{1}{N} \sum_{\mathbf{R}_{X_2'}, \mathbf{R}_{X_1}} -t\big(\mathbf{R}_{X_2'} - \mathbf{R}_{X_1}\big) \exp\left[-i\mathbf{k}' \cdot \mathbf{R}_{X_2'} + i\mathbf{k} \cdot \mathbf{R}_{X_1}\right] \\
&\quad = \frac{1}{N} \sum_{\mathbf{R}_{X_2'}, \mathbf{R}_{X_1}} -t\big(\mathbf{R}_{X_2'} - \mathbf{R}_{X_1}\big) \\
&\qquad \times \exp\left[-i\bar{\mathbf{k}} \cdot \big(\mathbf{R}_{X_2'} - \mathbf{R}_{X_1}\big)\right] \exp\left[-i\,\Delta\mathbf{k} \cdot \frac{\mathbf{R}_{X_2'} + \mathbf{R}_{X_1}}{2}\right],
\end{aligned} \tag{A1}$$

where

$$\bar{\mathbf{k}} = \frac{\mathbf{k}+\mathbf{k}'}{2}, \quad \Delta\mathbf{k} = \mathbf{k}' - \mathbf{k}. \tag{A2}$$

Since the Moire lattice constant L_{M} is much larger than a in TBGs with small rotation angles, we need to consider only $\mathbf{k}$ and $\mathbf{k}'$ which are close to each other, or $|\Delta\mathbf{k}| \ll 2\pi/a$. Then the last exponential term in Eq. (A1) is slowly varying in space, while the other terms change in the atomic length scale. To separate out the long-wave component, we introduce a smoothing function $g(\mathbf{r})$ which satisfies the following conditions:[59] $g(\mathbf{r})$ varies in $\mathbf{r}$ in an intermediate length scale l_g, which is much larger than the lattice constant a but much smaller than the Moiré superlattice period L_{M}. $g(\mathbf{r})$ is a peak centered at $\mathbf{r}=0$ and rapidly decays in $\mathbf{r} \gtrsim l_g$. The area is normalized as

$$\int g(\mathbf{r})d\mathbf{r} = \Omega_{\mathrm{M}}, \tag{A3}$$

where Ω_{M} is the Moiré superlattice unit cell, and the integral is taken over the whole system area unless otherwise stated. Almost equivalently, we have

$$\sum_{\mathbf{R}_X} g(\mathbf{r}-\mathbf{R}_X) = \frac{\Omega_{\mathrm{M}}}{\Omega_0}, \tag{A4}$$

where X is of either A_1, B_1, A_2, or B_2, and $\Omega_0 = |\mathbf{a}_1 \times \mathbf{a}_2|$ is the area of the monolayer's unit cell.

Using Eq. (A4), the matrix element, Eq. (A1), is written as

$$\begin{aligned}\langle \mathbf{k}', X_2'|H|\mathbf{k}, X_1\rangle &= \frac{1}{N}\sum_{\mathbf{R}_{X_2'},\mathbf{R}_{X_1}}\left[\frac{1}{\Omega_{\mathrm{M}}}\int g(\mathbf{r}-\mathbf{R}_{X_1})d\mathbf{r}\right]\left[-t(\mathbf{R}_{X_2'}-\mathbf{R}_{X_1})\right] \\ &\quad\times \exp\left[-i\bar{\mathbf{k}}\cdot(\mathbf{R}_{X_2'}-\mathbf{R}_{X_1})\right]\exp\left[-i\Delta\mathbf{k}\cdot\frac{\mathbf{R}_{X_2'}+\mathbf{R}_{X_1}}{2}\right].\end{aligned} \tag{A5}$$

Now the argument $(\mathbf{R}_{X_2'}+\mathbf{R}_{X_1})/2$ in Eq. (A5) can be replaced with $\mathbf{R}_{X_1}$, because the last exponential term varies slowly with the length scale of L_{M}, and also the hopping integral $t(\mathbf{R}_{X_2'}-\mathbf{R}_{X_1})$ occurs only in the atomic scale distance. This is further replaced with $\mathbf{r}$, since the smoothing factor $g(\mathbf{r}-\mathbf{R}_{X_1})$ works as the δ function for the slowly varying function with the scale L_{M}. By including this, we obtain

$$\begin{aligned}\langle \mathbf{k}', X_2'|H|\mathbf{k}, X_1\rangle &\approx \frac{1}{N\Omega_{\mathrm{M}}}\int d\mathbf{r}\, e^{-i\Delta\mathbf{k}\cdot\mathbf{r}}\sum_{\mathbf{R}_{X_1}} g(\mathbf{r}-\mathbf{R}_{X_1}) \\ &\quad\times\sum_{\mathbf{R}_{X_2'}}\left[-t(\mathbf{R}_{X_2'}-\mathbf{R}_{X_1})\right]\exp\left[-i\bar{\mathbf{k}}\cdot(\mathbf{R}_{X_2'}-\mathbf{R}_{X_1})\right] \\ &= \frac{1}{\Omega_{\mathrm{M}}}\int_{\Omega_{\mathrm{M}}} d\mathbf{r}\, e^{-i\Delta\mathbf{k}\cdot\mathbf{r}}U_{X_2'X_1}[\bar{\mathbf{k}},\boldsymbol{\delta}(\mathbf{r})],\end{aligned} \tag{A6}$$

where we used Eq. (A4) and $\int d\mathbf{r}/(N\Omega_0) = \int_{\Omega_{\mathrm{M}}} d\mathbf{r}/\Omega_{\mathrm{M}}$. The last equation is the final result of Eq. (16).

---

[1] C. Berger, Z. Song, X. Li, X. Wu, N. Brown, C. Naud, D. Mayou, T. Li, J. Hass, A. N. Marchenkov *et al.*, Science **312**, 1191 (2006).

[2] Z. Ni, Y. Wang, T. Yu, Y. You, and Z. Shen, Phys. Rev. B **77**, 235403 (2008).

[3] Z. Yan, Z. Peng, Z. Sun, J. Yao, Y. Zhu, Z. Liu, P. M. Ajayan, and J. M. Tour, ACS Nano **5**, 8187 (2011).

[4] L. Xie, H. Wang, C. Jin, X. Wang, L. Jiao, K. Suenaga, and H. Dai, J. Am. Chem. Soc. **133**, 10394 (2011).

[5] R. Zhao, Y. Zhang, T. Gao, Y. Gao, N. Liu, L. Fu, and Z. Liu, Nano Res. **4**, 712 (2011).

[6] J. Hass, R. Feng, J. Millan-Otoya, X. Li, M. Sprinkle, P. First, W. De Heer, E. Conrad, and C. Berger, Phys. Rev. B **75**, 214109 (2007).

[7] J. Hass, F. Varchon, J. Millan-Otoya, M. Sprinkle, N. Sharma, W. de Heer, C. Berger, P. First, L. Magaud, and E. Conrad, Phys. Rev. Lett. **100**, 125504 (2008).

[8] G. Li, A. Luican, J. Dos Santos, A. Neto, A. Reina, J. Kong, and E. Andrei, Nat. Phys. **6**, 109 (2009).

[9] D. Miller, K. Kubista, G. Rutter, M. Ruan, W. de Heer, P. First, and J. Stroscio, Phys. Rev. B **81**, 125427 (2010).

[10] A. Luican, G. Li, A. Reina, J. Kong, R. Nair, K. Novoselov, A. Geim, and E. Andrei, Phys. Rev. Lett. **106**, 126802 (2011).

[11] J. Lopes dos Santos, N. Peres, and A. Castro Neto, Phys. Rev. Lett. **99**, 256802 (2007).

[12] E. Morell, J. Correa, P. Vargas, M. Pacheco, and Z. Barticevic, Phys. Rev. B **82**, 121407 (2010).

[13] S. Shallcross, S. Sharma, E. Kandelaki, and O. Pankratov, Phys. Rev. B **81**, 165105 (2010).

[14] G. Trambly De Laissardière, D. Mayou, and L. Magaud, Nano Lett. **10**, 804 (2010).

[15] R. Bistritzer and A. MacDonald, Proc. Natl. Acad. Sci. USA **108**, 12233 (2011).

[16] J. M. B. Lopes dos Santos, N. M. R. Peres, and A. H. Castro Neto, Phys. Rev. B **86**, 155449 (2012).

[17] Z. Ni, L. Liu, Y. Wang, Z. Zheng, L. Li, T. Yu, and Z. Shen, Phys. Rev. B **80**, 125404 (2009).

[18] A. Righi, S. Costa, H. Chacham, C. Fantini, P. Venezuela, C. Magnuson, L. Colombo, W. Bacsa, R. Ruoff, and M. Pimenta, Phys. Rev. B **84**, 241409 (2011).

[19] K. Sato, R. Saito, C. Cong, T. Yu, and M. S. Dresselhaus, Phys. Rev. B **86**, 125414 (2012).

[20] J. T. Robinson, S. W. Schmucker, C. B. Diaconescu, J. P. Long, J. C. Culbertson, T. Ohta, A. L. Friedman, and T. E. Beechem, ACS Nano **7**, 637 (2013).

[21] Y. Wang, Z. Ni, L. Liu, Y. Liu, C. Cong, T. Yu, X. Wang, D. Shen, and Z. Shen, ACS Nano **4**, 4074 (2010).

[22] T. Ohta, T. E. Beechem, J. T. Robinson, and G. L. Kellogg, Phys. Rev. B **85**, 075415 (2012).

[23] X. Zou, J. Shang, J. Leaw, Z. Luo, L. Luo, C. La-o vorakiat, L. Cheng, S. A. Cheong, H. Su, J.-X. Zhu *et al.*, Phys. Rev. Lett. **110**, 067401 (2013).

[24] R. Nair, P. Blake, A. Grigorenko, K. Novoselov, T. Booth, T. Stauber, N. Peres, and A. Geim, Science **320**, 1308 (2008).
[25] Z. Li, E. Henriksen, Z. Jiang, Z. Hao, M. Martin, P. Kim, H. Stormer, and D. N. Basov, Nat. Phys. **4**, 532 (2008).
[26] K. F. Mak, M. Y. Sfeir, Y. Wu, C. H. Lui, J. A. Misewich, and T. F. Heinz, Phys. Rev. Lett. **101**, 196405 (2008).
[27] L. Zhang, Z. Li, D. Basov, M. Fogler, Z. Hao, and M. Martin, Phys. Rev. B **78**, 235408 (2008).
[28] E. Henriksen, Z. Jiang, L.-C. Tung, M. Schwartz, M. Takita, Y.-J. Wang, P. Kim, and H. Stormer, Phys. Rev. Lett. **100**, 87403 (2008).
[29] Z. Li, E. Henriksen, Z. Jiang, Z. Hao, M. C. Martin, P. Kim, H. Stormer, and D. N. Basov, Phys. Rev. Lett. **102**, 37403 (2009).
[30] Y. Zhang, T.-T. Tang, C. Girit, Z. Hao, M. C. Martin, A. Zettl, M. F. Crommie, Y. R. Shen, and F. Wang, Nature **459**, 820 (2009).
[31] M. Orlita, C. Faugeras, J. M. Schneider, G. Martinez, D. K. Maude, and M. Potemski, Phys. Rev. Lett. **102**, 166401 (2009).
[32] A. Kuzmenko, E. van Heumen, D. van der Marel, P. Lerch, P. Blake, K. Novoselov, and A. Geim, Phys. Rev. B **79**, 115441 (2009).
[33] A. Kuzmenko, I. Crassee, D. Van der Marel, P. Blake, and K. Novoselov, Phys. Rev. B **80**, 165406 (2009).
[34] K. F. Mak, M. Y. Sfeir, J. A. Misewich, and T. F. Heinz, Proc. Natl. Acad. Sci. USA **107**, 14999 (2010).
[35] K. F. Mak, J. Shan, and T. F. Heinz, Phys. Rev. Lett. **104**, 176404 (2010).
[36] T. Ando, Y. Zheng, and H. Suzuura, J. Phys. Soc. Jpn. **71**, 1318 (2002).
[37] V. Gusynin and S. Sharapov, Phys. Rev. B **73**, 245411 (2006).
[38] V. Gusynin, S. Sharapov, and J. Carbotte, Phys. Rev. Lett. **96**, 256802 (2006).
[39] V. Gusynin, S. Sharapov, and J. Carbotte, Phys. Rev. Lett. **98**, 157402 (2007).
[40] D. Abergel and V. Fal'ko, Phys. Rev. B **75**, 155430 (2007).
[41] L. Falkovsky and S. Pershoguba, Phys. Rev. B **76**, 153410 (2007).
[42] M. Koshino and T. Ando, Phys. Rev. B **77**, 115313 (2008).
[43] M. Koshino and T. Ando, Solid State Commun. **149**, 1123 (2009).
[44] N. Peres, Rev. Mod. Phys. **82**, 2673 (2010).
[45] M. Koshino, New J. Phys. **15**, 015010 (2013).
[46] Z. Chen and X. Wang, Phys. Rev. B **83**, 081405 (2011).
[47] C. J. Tabert and E. J. Nicol, Phys. Rev. B **87**, 121402 (2013).
[48] E. Mele, Phys. Rev. B **81**, 161405 (2010).
[49] E. Mele, J. Phys. D: Appl. Phys. **45**, 154004 (2012).
[50] T. A. Green and J. Weigle, Helv. Phys. Acta **21**, 217 (1948).
[51] T. Nakanishi and T. Ando, J. Phys. Soc. Jpn. **70**, 1647 (2001).
[52] S. Uryu, Phys. Rev. B **69**, 075402 (2004).
[53] J. Slater and G. Koster, Phys. Rev. **94**, 1498 (1954).
[54] M. Kindermann and P. First, Phys. Rev. B **83**, 045425 (2011).
[55] J. McClure, Phys. Rev. **104**, 666 (1956).
[56] D. DiVincenzo and E. Mele, Phys. Rev. B **29**, 1685 (1984).
[57] G. Semenoff, Phys. Rev. Lett. **53**, 2449 (1984).
[58] N. H. Shon and T. Ando, J. Phys. Soc. Jpn. **67**, 2421 (1998).
[59] T. Ando, J. Phys. Soc. Jpn. **74**, 777 (2005).
[60] T. Ando, J. Phys. Soc. Jpn. **38**, 989 (1975).
[61] S. Latil, V. Meunier, and L. Henrard, Phys. Rev. B **76**, 201402 (2007).
[62] S. Shallcross, S. Sharma, and O. Pankratov, Phys. Rev. Lett. **101**, 56803 (2008).
[63] M. Sprinkle, D. Siegel, Y. Hu, J. Hicks, A. Tejeda, A. Taleb-Ibrahimi, P. Le Fèvre, F. Bertran, S. Vizzini, H. Enriquez *et al.*, Phys. Rev. Lett. **103**, 226803 (2009).
[64] P. Moon and M. Koshino, Phys. Rev. B **85**, 195458 (2012).
[65] T. Ohta, J. Robinson, P. Feibelman, A. Bostwick, E. Rotenberg, and T. Beechem, Phys. Rev. Lett. **109**, 186807 (2012).